



Nitrogen vacancies regulated the local electron density of iron sites in g-C₃N₄ to boost the generation of high-valent iron-oxo species in a peracetic acid-based Fenton-like process

Junyan Kuang^a, HaiJuan Guo^{b,*}, Qishi Si^a, Wanqian Guo^a, Fang Ma^{a,*}

^a State Key Laboratory of Urban Water Resource and Environment, School of Environment, Harbin Institute of Technology, Harbin 150090, PR China

^b School of Environment, Liaoning University, Shenyang 110036, PR China

ARTICLE INFO

Keywords:

Heterogeneous Fenton reaction
Nitrogen vacancy engineering
Peracetic acid
Nonradical oxidation
High-valent iron-oxo

ABSTRACT

Large-scale production of high-valent iron-oxo species (Fe(V)=O) for the efficient removal of organic pollutants has been a challenge due to the high activation energy barrier of the Fe(III)-oxidant complex. Here, we propose a novel heterogeneous system using Fe(III)-doped g-C₃N₄ with three-coordinate nitrogen vacancies (FNCN) as a catalyst for the activation of peracetic acid (PAA). Our investigations and calculations indicate that Fe(III) is the primary active site, and illustrate a nonradical mechanism of two-electron transfer mechanism to produce Fe(V)=O species. Meanwhile, the abundant nitrogen vacancies (Nvs) strengthen the electron distribution of the Fe(III) sites to promote reactivity, and reduce the energy barrier to break the O–O bond of PAA in the Fe(III)–PAA complex, to achieve the rapid accumulation of Fe(V)=O species. As a result, this heterogeneous system has excellent selectivity and anti-interference in removal of pollutants. Our work offers a unique viewpoint to strengthen a nonradical pathway in PAA activation.

1. Introduction

The selective removal of organic contaminants is an urgent issue, because these recalcitrant organics in water cause many substantial hazards to the ecosystem and public health, even at low concentrations [1]. Heterogeneous advanced oxidation processes (AOPs) have encouraging effectiveness for the elimination of organic contaminants in water [2–5]. Peracetic acid (PAA) is a strong oxidant with a redox potential of 1.06–1.96 V, which has been used for disinfection and oxidation in wastewater [6]. Chemically speaking, PAA is a fairly selective oxidant with a rate constant range from 3.2×10^{-6} to $> 1.0 \times 10^5 \text{ M}^{-1}\text{s}^{-1}$ [7]. Additionally, the bond energy of O–O in PAA is 159 kJ mol^{−1}, which can be thermally feasible to dissociate PAA and generate the reactive radicals [8–11]. Moreover, PAA's bond energy of O–O is lower than that of PMS (317 kJ mol^{−1}) and the routinely utilized H₂O₂ (213 kJ mol^{−1}) [12]. Various metals, including Fe(II/III), Co(II/III), Mn(II/III), Ni(II), Cu(II), and Ru(III), have been used to activate PAA for pollutants removal [13–16]. In general, it is commonly acknowledged that the primary mechanism is radical-induced oxidation during a variety of transition metal-based Fenton-like reactions. In radical-induced reactions, the one-electron transfer mechanism is often involved in the

activation of peroxides via homolytic peroxide bond (O–O) cleavage, which is linked to the continuous creation of radical species [17]. Similarly, a two-electron transfer mechanism can also occur in PAA activation initiate nonradical-mediated oxidation reactions. It has been reported that Fe(IV)=O species can provide a better long-lasting effect in water and can include a multiplicity of components to oxidize contaminants due to its slight vulnerability to scavengers compared to radicals such as •OH [18,19].

Some recent studies have discovered that the special redox characteristics of the central metal atom in metal coordination complexes with N-based ligands can be employed in a nonradical route when they are used to activate peroxide. Due to the stable structure and affordability of metal–N bond, the two-dimensional material graphitic carbon nitride (g-C₃N₄) has been widely researched in the purification of wastewater. More crucially, the catalytic performance is significantly improved when there are enough N atoms coordinated with different metals (such as Fe, Co, Mn, and Cu) [20–22]. Then, the oxidant can be activated through a unique nonradical pathway due to the exceptional redox properties of the central metal atom. For example, Li et al. proposed that PMS can undergo a two-electron process to convert Fe(III) to Fe(V) when Fe(III) is doped into g-C₃N₄ to activate PMS [23]. Liu et al. [24] created a

* Corresponding authors.

E-mail addresses: guohaijuan@163.com (H. Guo), mafang@hit.edu.cn (F. Ma).

<https://doi.org/10.1016/j.apcatb.2023.122990>

Received 18 March 2023; Received in revised form 9 June 2023; Accepted 10 June 2023

Available online 12 June 2023

0926-3373/© 2023 Published by Elsevier B.V.

g-C₃N₄ catalyst with Co(II) doping to activate PAA, and found that the Co(IV)=O species played a major role in sulfonamide removal. Jiang et al. [25] showed that a Fe(V)-dominant oxidation mechanism might also be driven by a single-atom Fe(III) in the presence of Fe-N-C coordination. We speculate that, due to similar characteristics of peroxides (PMS vs. PAA), PAA can be activated through a nonradical mechanism by Fe-doped g-C₃N₄ to produce high-valence iron-oxo species for water purification.

Recently, high-valent metal-oxo species-dominated AOPs have drawn much attention from researchers due to their excellent selectivity and superior anti-interference versus the traditional radical-dominated AOPs [26–28]. However, the high energy barrier of the intermediate metal-PAA complex cleaving the O–O bonds of PAA severely hinder the formation of high-valent metal-oxo species [29,30]. To date, not enough studies have been conducted to prove how Fe(V)=O can be rapidly and abundantly produced through electronic modulation strategies. Defect engineering strategies are commonly used to modify the electronic structure of catalysts [31]. Recently, Wang et al. [32] discovered that oxygen vacancy-rich ultrathin 2D Fe₃O₄ improved the electron transfer among pollutants and oxidants and noticeably reduced the energy barrier for interfacial charge transfer. Duan et al. prepared amorphous carbon nitride with N_{3C}-site vacancies (ACN3) as a photocatalyst to enhanced photocatalytic NO oxidation [33]. They proved that of N_{3C} vacancies can boost the light-harvesting capacity, decrease the bandgap and improve the charge separation. So, the removal of NO in ACN3 is higher than that of CN. Zhang et al. [34] designed a g-C₃N₄ with dual defect sites (–C≡N groups and N vacancies) to achieve ultrahigh photocatalytic H₂O₂ evolution. The material produces an electron-rich region, and leads to a more localized charge density distribution. Theoretical calculations have clearly shown that N defect sites can effectively activate O₂, while –C≡N sites enhance the adsorption of H⁺. According to Su et al. [35], designed nitrogen vacancies may act as electron trap sites, enabling photoelectrons to accumulate on single iron atoms, thereby greatly increasing the H₂O₂ conversion. Previous studies have shown that N vacancies in Fe-based catalysts provide abundant localized electrons for Fe sites, but it is unknown how these vacancies affect the formation of high-valent Fe(V)=O.

Our objectives for this research were to (1) propose a new non-radical mechanism for activating PAA using Fe(III) doped CN with N_{3C} vacancies (FNCN) for sulfamethoxazole (SMX) oxidation, (2) design three coordinate nitrogen vacancies (Nvs) into CN to accelerate the formation of Fe(V)=O species, (3) use density functional theory (DFT) calculations to thoroughly explain the roles of Fe(III) and Nvs in the PAA activation process, and (4) determine the transformation products and the toxicity of intermediates during the abatement of SMX. Additionally, the study also measured the degradation kinetics, the impact of the evaluation effects (pH, FNCN dosages, PAA dosages) and the reusability of FNCN catalyst in the removal performance of SMX.

2. Experimental section

2.1. Materials

Text S1 has detailed information on the substances utilized.

2.2. Fabrication of Fe(III) doped Nvs-g-C₃N₄

The Fe(III) doped g-C₃N₄ with N_{3C} vacancies was fabricated by combining various concentrations of FeCl₃·6 H₂O with 0.5 g ammonium acetate and urea (10 g) in 50 mL deionized water. The solvents were then vaporized overnight in a vacuum oven at 80 °C after the mixed solution had been agitated for 10 h. Afterward, the mixture was heated to 550 °C with a heating rate of 5 °C min^{−1} and kept for 2 h in a muffle furnace. A series of Fe(III) doped g-C₃N₄ with N_{3C} vacancies samples were denoted as FNCNx, where x = 1, 2, 3, 4, and 5, matching the different dosages of FeCl₃·6 H₂O (0.25, 0.5, 1, 1.5 and 2.0 mmol),

respectively. As a comparison, the bulk g-C₃N₄ was made by heating the urea (10 g) according to the same experimental protocol, which denoted as CN. The same process was used to create the g-C₃N₄ with N_{3C} vacancies, named as NCN, but without FeCl₃·6 H₂O in the solution. The procedure of FNCNx heterojunctions photocatalysts is proposed as illustrated in Fig. S1.

2.3. Characterization

Text S2 has detailed information on the characterization of samples. The identification of ROS has detailed in Text S3.

2.4. Catalytic processes

All the catalytic processes were carried out at room temperature (26 °C) and wrapped in tin foil to keep out the light with magnetic stirring. Target organic compounds like SMX and PAA solutions in preplanned quantities were initially introduced to the system with or without substrates, and the total solution volume was 100 mL. The pH was changed by adding 0.5 M H₂SO₄ or NaOH reserve liquid for single-factor tests to investigate the implications of pH from 2 to 9. Following the addition of equal volumes of sodium thiosulfate solution (1 mL, 500 mM) to quenched 1 mL samples which were taken at predetermined intervals. After extracted the solid components via a 0.22 μm membrane, and then, the remaining concentration of the target organic compound was quantified by HPLC.

2.5. Computational method

The Gaussian 09 software was used to do DFT calculations (Revision D.01) and Text S4 shows more extensive information.

3. Results and discussion

3.1. Characterization of catalysts

The synthesis procedures of FNCNx are depicted in Figs. 1a and S1. FeCl₃, urea, and ammonium acetate were used as precursors in a facile one-step calcination process to create Fe(III)-doped g-C₃N₄ with Nvs. Electron paramagnetic resonance (EPR) spectra could be utilized to reveal the existence of Nvs. As seen in Fig. 1b, the electrons trapped in the Nvs on graphite NCN showed a slight Lorentz signal peak at a g value close to 2.0034 in fresh CN [36]. Obviously, the intensity of NCN increased noticeably, demonstrating the successful introduction of Nvs through the addition of ammonium acetate. By adding Fe(III), EPR signals of CN and NCN may be suppressed, proving that Fe(III) ions alter the localized spin of CN and NCN [37]. The crystalline phase structures of all samples were determined by XRD analysis in Fig. 1c. The weak diffractions at 13.2° and 27.7° belong to CN (100) and (002), respectively [38], which can be detected in all the samples. These diffractions are caused by the in-plane reflection and interlayer stacking of the conjugated aromatic rings. In the presence of ammonium acetate, the peaks at 13.2° of NCN and FNCN3 are apparently broadened and reduced, revealing that the in-plane long-range order was broken [39]. The chaotic in-plane structure then produced variations in the interlayer structure, which caused an amorphous structure in CN. In addition, the major peaks of all FNCNx samples only showed minor changes towards higher diffraction angles, accompanied by a slight decrease in intensity (Fig. S2), showing that Fe was satisfactorily incorporated into the framework of CN [40]. Interestingly, as evidenced by the absence of any XRD signal for Fe oxides such as Fe₂O₃, Fe₃O₄, or FeOOH, Fe(III) was chemically bonded with CN, presumably in the formation of Fe-N bonds.

The functional group structures of diverse materials were assessed by using FT-IR. As illustrated in Fig. 1d, a sequence of N–C≡N stretching vibration peaks with powerful adsorption were found in the range of 1743–1143 cm^{−1}. Peaks in the range of 3380–3052 cm^{−1} were classified

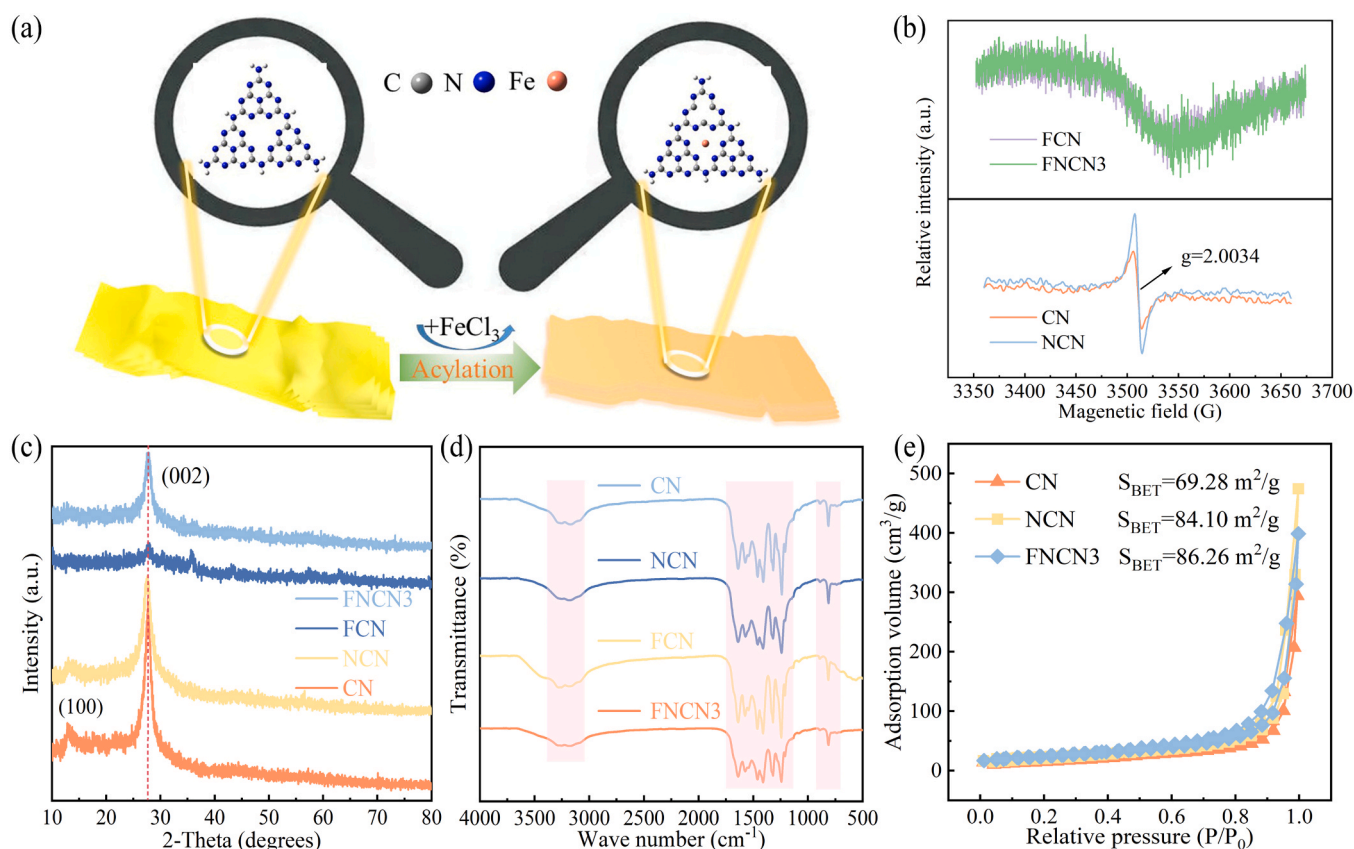


Fig. 1. Diagrammatic description of the creation of the FNCNx with N₃C vacancies (a). ESR (b), XRD (c), and FT-IR patterns (d) of CN, NCN, FCN, and FNCN3, respectively. Nitrogen adsorption-desorption isotherms of CN, NCN, and FNCN3, respectively (e).

as $\text{--NH}_2/\text{=NH}$ groups [41]. Additionally, a noticeable peak at 810 cm^{-1} corresponded to the stretching vibration of the out-of-plane bending mode of the heptazine rings system revealing that NCN and FNCN3 samples maintained their original CN atomic structures (C_6N_7) [42] after the addition of Nvs and Fe(III). Fig. S3d depicts the uniformly distributed nanostructure with an irregular and porous structure which can be attributed to the acylation reaction of certain Nvs production, which was advantageous for the deposition and distribution of metal elements. The findings from the SEM observation are further supported by TEM images (Fig. S4, Supporting Information). Meanwhile, TEM images reveal that all the samples are nanosheet structures, and the thickness of single-layer in FNCN3 was 1.95 nm (Fig. S5). The element mappings of FNCN3 in Fig. S6 demonstrate that Fe elements are uniformly distributed in FNCN3. Additionally, it is possible to demonstrate the presence of N vacancies by comparing the ratio of N components between CN and NCN. The meso/macropores is also illustrated by a nitrogen adsorption-desorption isotherm. The pore distribution and specific surface area of FNCN3 were 10.76 nm and $86.26\text{ m}^2\text{g}^{-1}$, respectively, as illustrated in Figs. S7 and 1e. The major mechanism for producing the porous structure was considered to be the acylation reaction between ammonium acetate and urea [43]. During the calcination of an amide molecule, vast quantities of CO_2 and NH_3 were released, creating a porous network structure. In summary, a simple thermal polymerization process was established to produce amorphous FNCN3 by breaking the in-plane hydrogen bonds of CN, and to mainly bind elemental Fe to the host CN instead of Fe oxides.

As illustrated in Fig. 2, the surface elemental composition and chemical states of the catalysts were discovered using XPS spectra. In the survey XPS analysis of all the catalyst, the indications of C, N, and O were detected, determining that the absorbed $\text{O}_2/\text{H}_2\text{O}$ was responsible for the minimal oxygen element (5%) [21]. The sp^2 hybridized carbon in

$\text{N}=\text{C}=\text{N}$, and the sp^3 graphitic carbon were created during the polymerization process in the C 1s spectra of FNCN3 (Fig. 2b), which were centered at 284.88 and 287.99 eV , respectively [44]. For C 1s of FCN and FNCN3, there was no chemical change after Fe doping. Interestingly, the N/C ratio decreased from 1.220 (pristine CN) to 1.065 (NCN) and 1.138 (FNCN3), as shown in Table S4. The decrease of N elements is evidence that the Nvs are successfully created in NCN and FNCN3. The high-resolution N 1s XPS peaks of fresh CN, NCN, FCN, and FNCN3 are shown in Fig. 2c-f. Three distinctive peaks could be found in the N 1s spectrum, which correspond to sp^2 hybridized N linked to C ($\text{C}=\text{N}-\text{C}$, N_2C), tertiary N ($\text{N}-\text{C}_3$), amino-functional groups ($\text{C}-\text{NH}_x$, $x = 1, 2$), and the heptazine ring [45,46]. As illustrated in Table S4, the percentage of $\text{N}_{3\text{C}}$ decreased from 15.1% for pristine CN to 12.9% for NCN, and reduced from 21.9% for FCN to 19.1% for FNCN3. Additionally, the ratio of $\text{N}_{2\text{C}}$ and $\text{N}_{3\text{C}}$ of NCN and FNCN3 was increased to 5.72 and 3.51 , clearly indicating that N vacancies could be created in the tertiary N site ($\text{N}-\text{C}_3$) (Fig. S9). Thus, samples with $\text{N}_{3\text{C}}$ -type N vacancies near Fe-N centers have been effectively constructed, providing a strong foundation for the future development of defect strategies to control the electron distribution of catalysts. Additionally, a discernible shift of N peaks was observed in FNCN3 compared to NCN (Table S4), indicating that the Fe insertion changed the chemical state of the hybridized aromatic. The minimal Fe components in the FNCN3 sample resulted in a faint Fe signal, and the valent states of the central Fe sites were investigated in Fig. 2g. The peaks toward 710.94 and 724.23 eV in the Fe 2p spectra of FNCN3 belonged to $\text{Fe } 2p_{3/2}$ and $\text{Fe } 2p_{1/2}$. In contrast to the XPS spectra of Fe_3O_4 , these peaks were placed at distinct energies (Fig. 2h) [47]. The binding energy of $\text{Fe } 2p_{3/2}$ was higher than that of Fe(II) phthalocyanine (709.2 eV) and located in the range of the Fe(III) valence state ($710.3\text{--}711.8\text{ eV}$) [40]. Meanwhile, the Fe 2p spectra of FNCN changed toward lower binding energy with the addition of Nvs (Fig. 2i),

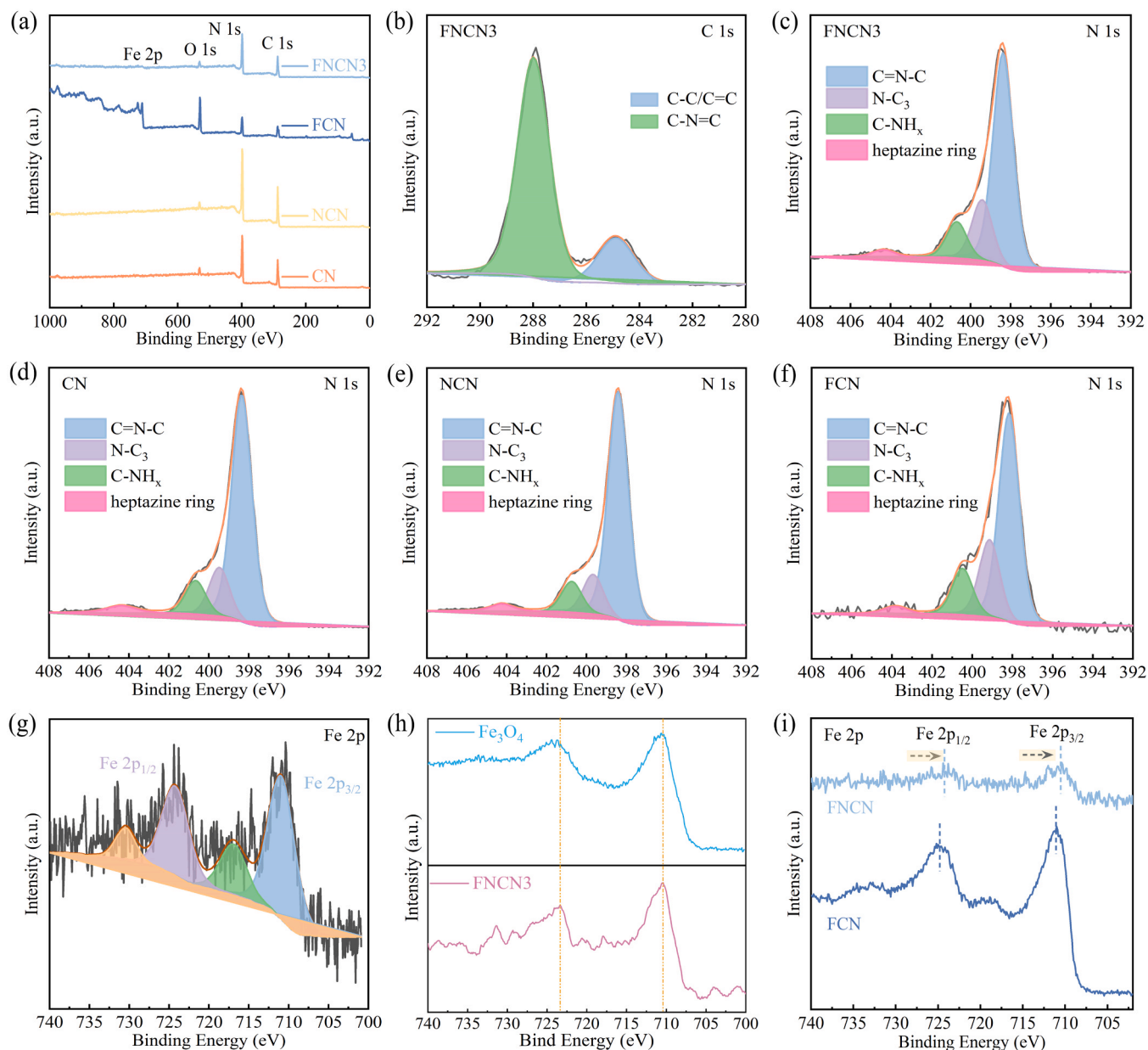


Fig. 2. Full-scale XPS spectra of CN, NCN, FCN, and FNCN3 (a). High-resolution C 1s XPS spectra of FNCN3 (b). High-resolution N 1s XPS spectra of FNCN3 (c), CN (d), NCN (e), and FCN (f), respectively. Fe 2p XPS spectra of FNCN3 (g). Fe 2p signals in FNCN3 or Fe₃O₄ (h). Fe 2p XPS spectra for FCN and FNCN3 (i).

demonstrating that Nvs were helpful to increase the local electron density around Fe sites [48]. These results revealed that Fe(III) and N atoms were effectively incorporated to create Fe(III)-N moieties, and it was reasonable to expect that Nvs would mostly be found at the N₃C joint sites.

3.2. Fenton-like performance of catalysts

The decontamination capabilities of the obtained FNCN3 were evaluated by removing SMX. The concentration of SMX did not change after 60 min in the PAA/SMX and only SMX systems, proving that the reduction of PAA and self-degradation of SMX could be avoided. The subsequent degradation of SMX in the FNCN3/PAA system was attributed to the Fenton-like process due to the negligible adsorption of SMX by FNCN3 (Fig. S10). The degradation of SMX in various systems was investigated in Fig. 3a. The removal efficiencies of 7.01% and 7.36% by CN and NCN showed limited catalytic activity for the degradation of SMX, indicating that neither C nor N atoms in fresh CN were the primary

active sites for the removal of SMX. After the Fe(III) modification, the catalytic activities of FCN and FNCN3 in SMX removal were increased. The degradation of SMX was found to improve with the increase of Fe (III) content in the catalysts. For instance, the FNCN1/PAA system only eliminated 65.61% of SMX, whereas the FNCN3/PAA system boosted this to ~100% (Fig. S11). As a result, the typical catalyst was decided to be FNCN3 for the following experiments. When identical concentrations of Fe(III) ions were used to catalyze the homogeneous reaction, the decontamination capability was comparable (Fig. S12). The maximum Fe leaching measured in 60 min was approximately 0.472 mg L⁻¹. As shown by the fact that only approximately 13% of the SMX degradation was attributed to the leaching solution, indicating that the SMX removal was primarily caused by a heterogeneous reaction in the FNCN3/PAA system (Fig. S13).

The pseudo-first-kinetic analysis is depicted in Fig. 3b, and the reaction rates of CN, NCN, FCN, and FNCN3 are 0.0009, 0.0011, 0.0156, and 0.0759 min⁻¹, respectively. In addition, 11.1% and 15.7% of PAA was consumed by CN and NCN, respectively, while FCN and FNCN3

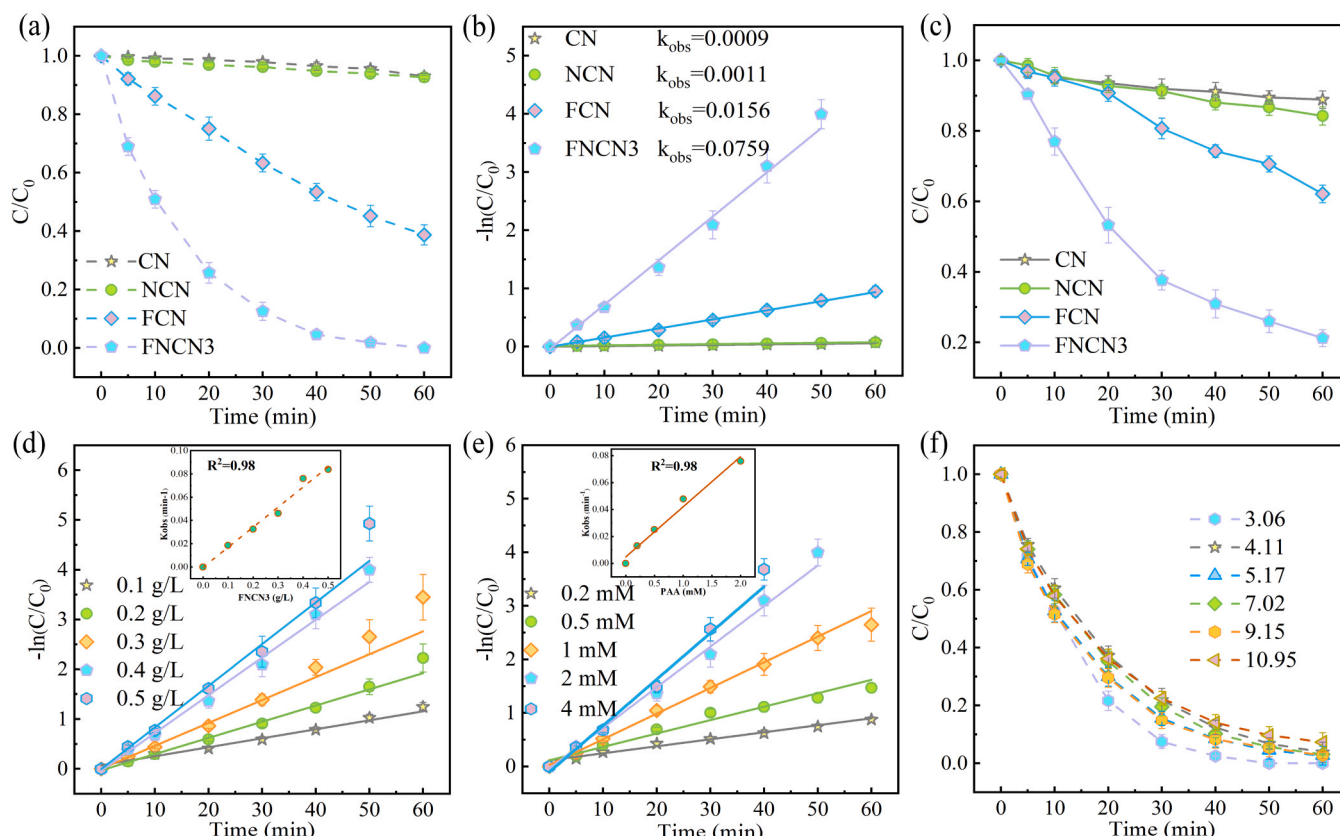


Fig. 3. Removal of SMX with CN, NCN, FCN, and FNCN3 (a). The corresponding linear relationship of $-\ln(C/C_0)$ versus reaction time (b). The consumption of PAA in different systems (c). Pseudo-first-order kinetic fitting on SMX degradation at different FNCN3 dosages (d) and PAA concentrations (e). Inset displays the overall rates (k) for SMX oxidation as a function of FNCN3 and PAA dosages. Degradation of SMX at different initial pH values in the FNCN3/PAA system (f). Reaction conditions are as follows: $[SMX]_0 = 10 \text{ mg L}^{-1}$, $[PAA]_0 = 2.0 \text{ mM}$, $[catalyst]_0 = 0.4 \text{ g L}^{-1}$, $\text{pH}_{\text{initial}} = 7.2$, and $T = 25^\circ\text{C}$.

consumed 37.9% and 78.8% of PAA, showing that Fe(III) was the primary site of PAA activation, and the presence of Nvs promoted the decomposition of PAA. Fig. 3d illustrates that the kinetics of SMX degradation in 60 min fits to the pseudo-first-order model for different dosages of FNCN3. With increase dosages of FNCN3 from 0.1 to 0.5 g L^{-1} , the rate constant (k) of SMX removal rose from 0.0181 to 0.0837 min^{-1} . A linear relationship between the FNCN3 dosages and k was observed (inset in Fig. 3d) with a coefficient of 0.98, demonstrating that the oxidation of SMX occurred on the surface of FNCN3. When a higher dosage of FNCN3 was employed, more active sites could be provided for the activation of PAA, resulting in increased subsequent SMX degradation. Additionally, when the PAA dose was raised from 0.2 to 4 mM, k increased from 0.0131 to 0.0866 min^{-1} (Fig. 3e). The fact that PAA was also a required component for the oxidation of SMX in FNCN3/PAA system, that was confirmed by the linear connection between k and the PAA concentrations (0.2–2 mM) with a coefficient of 0.98 (inset in Fig. 3e). The best options from an economic standpoint for the following tests were 2 mM PAA and 0.4 g L^{-1} FNCN3. Fig. 3f illustrates how the initial solution pH (3.06–10.95) affected the degradation of SMX in the FNCN3/PAA system. The SMX degradation efficiency was maintained between 96.19% and 97.33% at different initial pH values, demonstrating the superior pH flexibility of the FNCN3/PAA system.

The elimination of organic pollutants in actual water bodies is usually suppressed by some background substances such as inorganic anions and natural organic matter. As shown in Fig. S15a, a high level of SMX degradation (70% in 60 min) was still observed even when the concentration of HA reached 10 mg L^{-1} . Meanwhile, Cl^- accelerates the reactive rate, SO_4^{2-} has no inhibitory effect on the degradation effect of SMX in the FNCN3/PAA system, and the presence of NO_3^- has a slight effect on SMX degradation. However, HCO_3^- significantly inhibits the

degradation efficiency of SMX, the reason is that HCO_3^- will affect the decomposition of PAA during the activated process [49]. As shown in Fig. S16, the degradation efficiency of SMX in tap water is extremely close to the obtained for deionized water. For actual application in water treatment, though the removal of SMX in Man-made Lake and in Songhua River were modestly retarded, as high as 80.2% and 73.2% of SMX can be eliminated in FNCN3/PAA process within 60 min

3.3. Identification of oxidative species

The predominant oxidative species were thoroughly examined to clarify the mechanism of SMX elimination in the FNCN3/PAA system. First, the role of active species in the FNCN3/PAA system could be detected by free radical quenching experiments in Figs. 4a and S20. In PAA-based AOPs, $\bullet\text{OH}$ and $\text{R-O}\bullet$ (i.e., $\text{CH}_3\text{CO}_2\bullet$ and $\text{CH}_3\text{CO}_3\bullet$) are often considered to be active species to remove organic contaminants [50,51], and TBA and β -carotene can be used to identify them due to their distinct rate constants of quenching reactions. Fig. S20a demonstrates that the SMX degradation effect in the FNCN3/PAA system was not inhibited by TBA at concentrations ranging from 10 mM to 50 mM. Even when the TBA concentration was increased to 250 mM, the degradation effect of SMX still reached $\sim 81\%$, indicating that the elimination of SMX in the FNCN3/PAA process was not significantly influenced by $\bullet\text{OH}$. β -carotene reacts readily with $\text{CH}_3\text{CO}_3\bullet$ ($9.2 \times 10^8 \text{ M}^{-1}\text{s}^{-1}$), so it can effectively prevent $\text{CH}_3\text{CO}_3\bullet$ from interacting with SMX [52]. In comparison, the degradation of SMX was reduced by 23.1% when 10 mM β -carotene was added, which appears to be proof of the existence of $\text{R-O}\bullet$. Nevertheless, the weak inhibition effect of β -carotene also indicates that $\text{R-O}\bullet$ is not the main active species for SMX removal in FNCN3/PAA system. To this, conventional free radicals

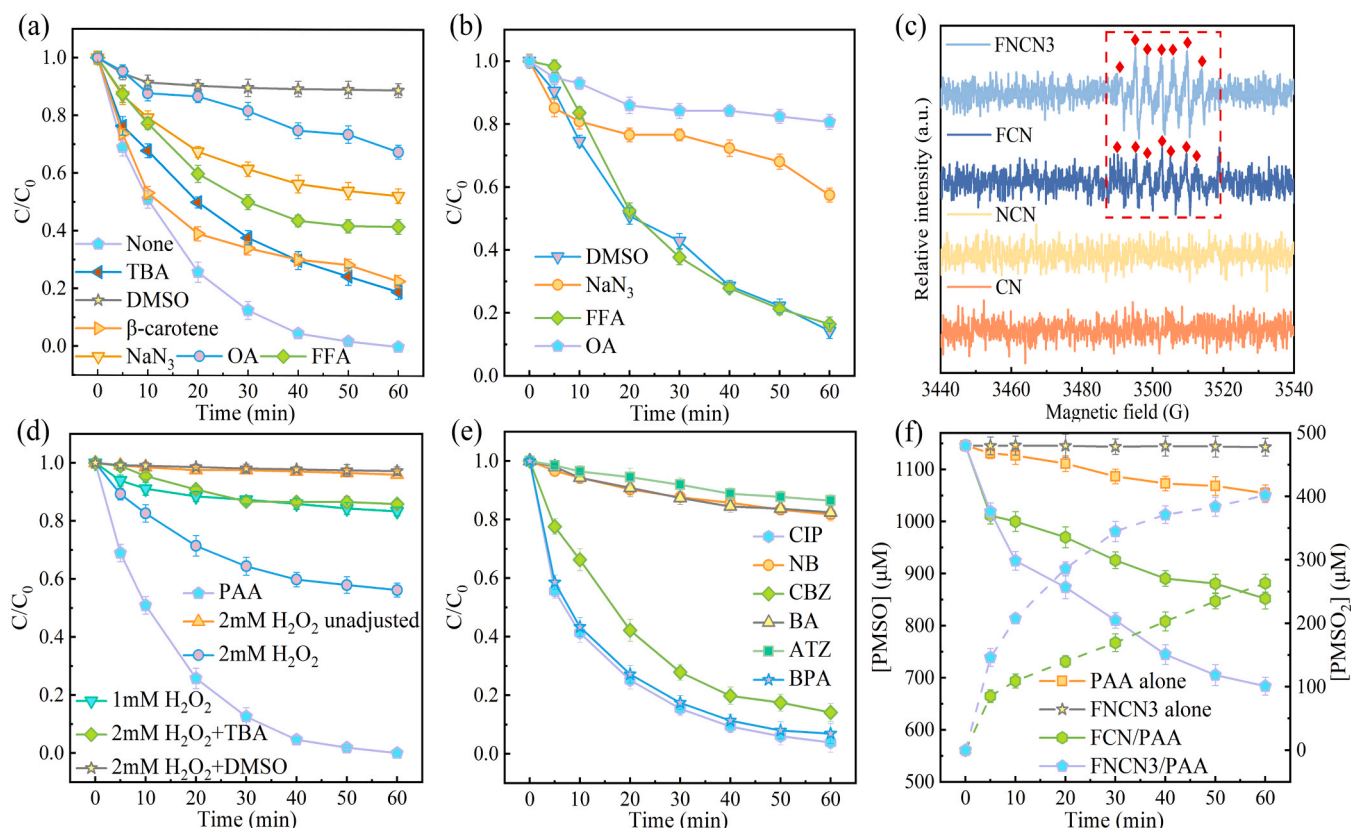


Fig. 4. SMX degradation (a) and PAA decomposition (b) with various scavengers in FNCN3 system. DMPO-trapping EPR signals in the FNCN3/PAA system after 5 min under different systems (c). Degradation of SMX in different FNCN3/ H_2O_2 systems (d). Selective oxidation of different contaminants in the FNCN3/PAA process (e). Decline of PMSO and production of PMSO₂ in the FCN/PAA or FNCN3/PAA process (f). Reaction conditions are as follows: [substrate]₀ = 10 mg L⁻¹, [PAA]₀ = 2.0 mM, [catalyst]₀ = 0.4 g L⁻¹, $\text{pH}_{\text{initial}}$ = 7.2, T = 25 °C, [DMSO] = [TBA] = 250.0 mM, [FFA] = [NaN_3] = 5.0 mM, and [β -carotene] = [OA] = 5.0 mM.

are not the primary active substances for SMX degradation, so non-radical oxidation is thought to be an important process in the FNCN3/PAA system. It can be seen from Fig. S20a that increasing the concentration of DMSO significantly hindered the elimination of SMX, and 250 mM DMSO nearly totally blocked 89% of SMX in the degradation process. Although DMSO was also found to effectively eliminated the ROS ($\bullet\text{OH}$ and $\text{HO}_2\bullet$) during the FNCN3/PAA process. But the inhibitory effect of TBA on SMX degradation was weak, even at higher concentrations. These results suggest that the inhibitory effect of DMSO on SMX degradation was not due to the quenching of ROS. Moreover, the inhibition effect of TBA and DMSO on the degradation of SMX in FCN/PAA system is similar to that of FNCN3/PAA system (Fig. S21). Some studies have reported that high-valent iron-oxo species (such as Fe(V)=O) could be produced in Fe(III)-N/PMS [23,53] and Fe(III)-N/ H_2O_2 system [54]. Nevertheless, it is not known whether SMX decomposition in the FNCN3/PAA process includes high-valent iron-oxo species. In contrast to the radical-based oxidation, sulfoxides (such as DMSO and dimethyl sulfoxide) can be oxidized by high-valent iron-oxo species to form the corresponding sulfones (such as DMSO₂ and dimethyl sulfone) via the oxygen-atom-transfer reaction [27]. Therefore, it was speculated that Fe(V)=O would serve as the main active species rather than radical species for SMX decomposition in the FNCN3/PAA process.

In the SMX degradation, FFA and NaN_3 are thought to be appropriate scavengers of singlet oxygen ($^1\text{O}_2$) ($k_{\text{FFA}} = 1.2 \times 10^8 \text{ M}^{-1}\text{s}^{-1}$ and $k_{\text{NaN}_3} = 1 \times 10^9 \text{ M}^{-1}\text{s}^{-1}$) [55]. As seen in Fig. S20b, increasing the concentrations of FFA and NaN_3 could greatly impeded the removal of SMX by FNCN3/PAA system. When the concentration of FFA and NaN_3 was 5 mM, the degradation efficiency of SMX was decreased to 58.3% and 47.7%, respectively. This finding suggested that $^1\text{O}_2$ may also be the active species for removing SMX in the FNCN3/PAA system. Chelating

agent such as oxalate (OA) was introduced to the FNCN3/PAA system to further support the critical function of Fe(III) in PAA activation. It is commonly recognized that the carboxyl groups of OA may combine with Fe(III) to generate a metal-carboxyl complex [56], which might inhibit the capacity of Fe(III) to activate PAA and thus reduce SMX degradation efficiency. Only 32.4% of SMX was eliminated by the FNCN3/PAA system with 10 mM OA in Fig. S20c, and the SMX decomposition steadily decreased as the increased quantity of OA. Fig. 4b depicts the consumption of PAA during the elimination of SMX when various trapping agents were added to the FNCN3/PAA system. The presence of NaN_3 had a significant impact on the activation of PAA by FNCN3, suggesting that NaN_3 reduced the degradation effect of SMX by preventing the decomposition of PAA rather than quenching $^1\text{O}_2$. Additionally, the inhibition of OA to the consumption of PAA was attributed to the formation of a metal-carboxyl complex, which prevents the PAA activation by FNCN3. However, the decomposition of PAA by FNCN3 was not affected by DMSO and FFA, indicating that their inhibition of SMX degradation was due to the quenching of active species. The aforementioned findings indicated that the FNCN3/PAA procedure did not employ a radical route to remove SMX. As a result, SMX decomposition in the FNCN3/PAA system relies on nonradical oxidation. In addition, the consumption of PAA and the oxidation of SMX may occurred at the Fe(III) sites in FNCN3.

Observations of electron spin resonance (EPR) under various situations validated these above findings. When DMPO was utilized as a trapping agent in Fig. 4c, neither the CN/PAA nor FNCN3/PAA systems showed well-defined peaks in the EPR spectra. Fascinatingly, no EPR signals of the DMPO-OH adduct could be discovered during the FCN/PAA and FNCN3/PAA processes, but a heptet signal authorized to 5,5-dimethyl-1-pyrrolidone-2-oxyl (DMPOX) peaks with a strength of

1:2:1:2:1:2:1 was detected under a typical response [57], suggesting that the FCN/PAA and FNCN3/PAA systems could directly oxidize DMPO. The fact that the intensity of DMPOX was much higher in the FNCN3/PAA system than in the FCN/PAA system provided further evidence that more DMPOX was produced during the FNCN3/PAA process. It was demonstrated that the formation of DMPOX was directly related to the main active species involved in the removal of SMX. Finally, there were only two primary hypotheses proposed for the origin of DMPOX: (i) DMPO is directly oxidized by a nonradical mechanism, and (ii) transient-life radical-DMPO adducts are rapidly synthesized. We assume that the oxidation of DMPO occurs through the nonradical reactions based on the above findings of the EPR spectra and the small inhibitory impact of TBA or β -carotene. Additionally, the H_2O_2 activation by FNCN3 were demonstrated in Fig. 4d. Only the "2 mM H_2O_2 unadjusted" system was performed at pH = 7.2, while other H_2O_2 activation systems were reacted at a pH = 3.6. The reason for choosing the condition of pH = 3.6 is that the pH of FNCN3/PAA system maintained at 3.66 during the degradation of SMX (Fig. S22). As can be seen from Fig. 4d, only 16.7% of SMX and 46.2% of SMX were degraded under the condition of 1 mM H_2O_2 and 2 mM H_2O_2 by FNCN3/ H_2O_2 system. In addition, TBA and DMSO were used as scavengers to verify the main active species in FNCN3/ H_2O_2 system. TBA could significantly inhibit the degradation of SMX, indicating that the main active species is $\bullet\text{OH}$ in FNCN3/ H_2O_2 system. The molar ratio of PAA/ H_2O_2 in the as-prepared PAA solution in this study is 1.24. Therefore, the above analysis confirms that the presence of H_2O_2 has no effect on the nonradical oxidation removal of SMX by the FNCN3/PAA system. The reactivity of FNCN3/PAA system under the typical micropollutants was also evaluated in Fig. 4e, below 20% of benzoic acid (BA), atrazine (ATZ) and nitrobenzene (NB) were removed, and carbamazepine (CBZ) was moderately degraded with the decay ratio of 85.8% in 60 min. In contrast, under same conditions, a complete elimination of bisphenol A (BPA) and ciprofloxacin (CIP) were realized within 60 min. The above results suggest that FNCN3/PAA system could oxidize various organic contaminants with different efficiencies. Similar selective degradation of pollutants was also occurred by nonradical oxidation in previous studies. Thus, due to the reactive sluggishness between CBZ and $\text{R}-\text{O}\bullet$, the SMX oxidation in FNCN3/PAA system was not a radical-based process.

According to the aforementioned experimental findings and other literature, nonradical mechanisms such as $^1\text{O}_2$, electron transfer, and high-valence metal oxides may contribute to the degradation of SMX in the FNCN3/PAA system. First, the TEMP-trapping research was performed to determine the role of $^1\text{O}_2$ in the FNCN3/PAA system. In Fig. S24a, PAA alone causes a distinct triplet signal of 2,2,6,6-tetramethyl-4-piperidinol-N-oxyl (TEMPO), which may be related to the self-decomposition of PAA. $\text{TEMP}-^1\text{O}_2$ adduct could be found in all the processes in EPR spectra, but there was no discernible transformation in the concentration of SMX during the CN/PAA and FNCN3/PAA systems. It is clear that the main reactive species responsible for the removal of SMX in FNCN3/PAA system was not $^1\text{O}_2$. Additionally, the theoretical maximum productivity is two moles of PAA producing one mole of $^1\text{O}_2$. Even though all PAAs were fully translated to $^1\text{O}_2$ under our conditions, according to the reaction rate constants of $^1\text{O}_2$ with SMX ($2 \times 10^4 \text{ M}^{-1} \text{ s}^{-1}$) and water ($2.5 \times 10^5 \text{ M}^{-1} \text{ s}^{-1}$), $^1\text{O}_2$ only represented less than 1% of the degradation of SMX [24], which was significantly lower than the actual finding (Test S4). In addition, changing H_2O into D_2O in FNCN3/PAA system is expected to kinetically promote SMX oxidation, because $^1\text{O}_2$ has a more than 10-fold higher lifetime in D_2O (20–32 μs) than in H_2O (2 μs) [58]. However, the rate of SMX decomposition (Fig. S24b). The above results discussed above proved that $^1\text{O}_2$ was produced, yet its role in the elimination of SMX during the FNCN3/PAA process could be disregarded. According to previous reports, the electron-transfer mechanism may be involved in heterogeneous oxidation. To monitor the current behavior in the FNCN3/PAA system, an amperometric i-t curve was performed, the introduction of PAA caused a

significant current surge in Fig. S25. However, unlike the normal electron transfer between PDS and carbon materials [59], there was no noticeable current response originating from the later injection of SMX in the case of FNCN3. In addition, PAA consumption in FCN/PAA and FNCN3/PAA systems with and without sulfamethoxazole have been tested in Fig. S26. Decline of PAA concentration was modestly decreased in the presence of SMX compared with that in the absence of SMX. This phenomenon is markedly different from the electron-transfer processes in the previous studies, among which the decline rate of peroxide significantly enhanced with the addition of pollutants (electron donor). Collectively, these findings suggest that electron transfer was not the primary mechanism for SMX elimination in the FNCN3/PAA system.

Overall, SMX oxidation in FNCN3/PAA system is dominated by a novel nonradical mechanism. Previous studies were typically supposed that high-valent iron-oxo species are often thought to be able to oxidize sulfoxides to thioketones, which are distinct from the product of oxidation by $\bullet\text{OH}$. In this work, the concentration of the product methyl phenyl sulfone (PMSO_2) was determined by using aromatic sulfoxide (PMSO) as the probe molecule [28]. As anticipated, a considerable amount of PMSO_2 was generated in the FCN/PAA and FNCN3/PAA system, and the conversion rate of PMSO to PMSO_2 was close to 100%, indicating that Fe(V)=O species were produced during the PAA activation. In general, Cl^- consume radical species (e.g., $\bullet\text{OH}$ and $\text{R}-\text{O}\bullet$) to produce chloride radicals with weaker oxidative capacity, thus exerting a more or less inhibition on the abatement of organic pollutants [60]. But, Fig. S15b shows Cl^- can accelerates the degradation of SMX in FNCN3/PAA system. Chen et al. confirmed that the Cl^- could be spontaneously oxidized to HClO by PAA. The cyclic relay of $\text{Fe}^{3+}-\text{Fe(V)=O}$ and Cl^--HClO substantially accelerated the electron transfer between BPA and PAA, which improved the catalytic performance toward BPA degradation [6]. Therefore, the promoting effect of Cl^- can also be confirmed the presence of Fe(V)=O in FNCN3/PAA system. Additionally, the decomposition amount of PMSO and the production amount of PMSO_2 in the FNCN3/PAA system were higher than those in the FCN/PAA system. Combined with the stronger peak signal of DMPOX in the EPR spectra, this suggests that more Fe(V)=O species were produced in the FNCN3/PAA system. Overall, the present results clearly supported the idea that Fe(V)=O species played a major role during the FNCN3/PAA process, and the existence of Nvs promoted the generation of active Fe(V)=O species.

3.4. Research on Fe–N active sites and significance of $\text{N}_{3\text{c}}\text{Vs}$

The incapacity of CN and FNCN in PAA decomposition (Fig. 3c) supports the conclusion that N-C compounds are poor samples for the PAA-based oxidation process (Fig. 2a). In contrast, the consumption of PAA was dramatically increased in the presence of FCN and FNCN3 were present, indicating the critical importance of the Fe–N sites in PAA activation. DFT calculations were used to determine the transition of Fe (III)-to- Fe(V)=O , as well as to clarify the modulation strategy of active species by Nvs. The optimization structural models of CN, FNCN, and FNCN3 are shown in Fig. S27. Fig. 5b shows the Bader charge of elements in CN and FNCN. Obviously, the insertion of Fe incorporated with the N sites changes the electron distribution of C and N atoms located around Fe sites in FCN and FNCN. This is attributed to the electropositive Fe atom taking electrons away from electronegative N atoms, resulting in a lower electron distribution for these N atoms and neighboring C atoms. Therefore, the insertion of Fe incorporated with N breaks the original chemical inertness of CN, which is helpful to improve the catalytic performance. The Bader charge analysis of FCN and FNCN in Fig. 5c shows that the designed $\text{N}_{3\text{c}}$ -type nitrogen vacancies further change the charge distribution. Most importantly, the electron density of the Fe atom is significantly strengthened by 0.29 e, indicating that Nvs favor the establishment of reaction centers for Fe with higher local electron densities, which is consistent with the results in Fig. 2i.

The adsorption of PAA on the interfaces of CN (Fig. S28a), FNCN

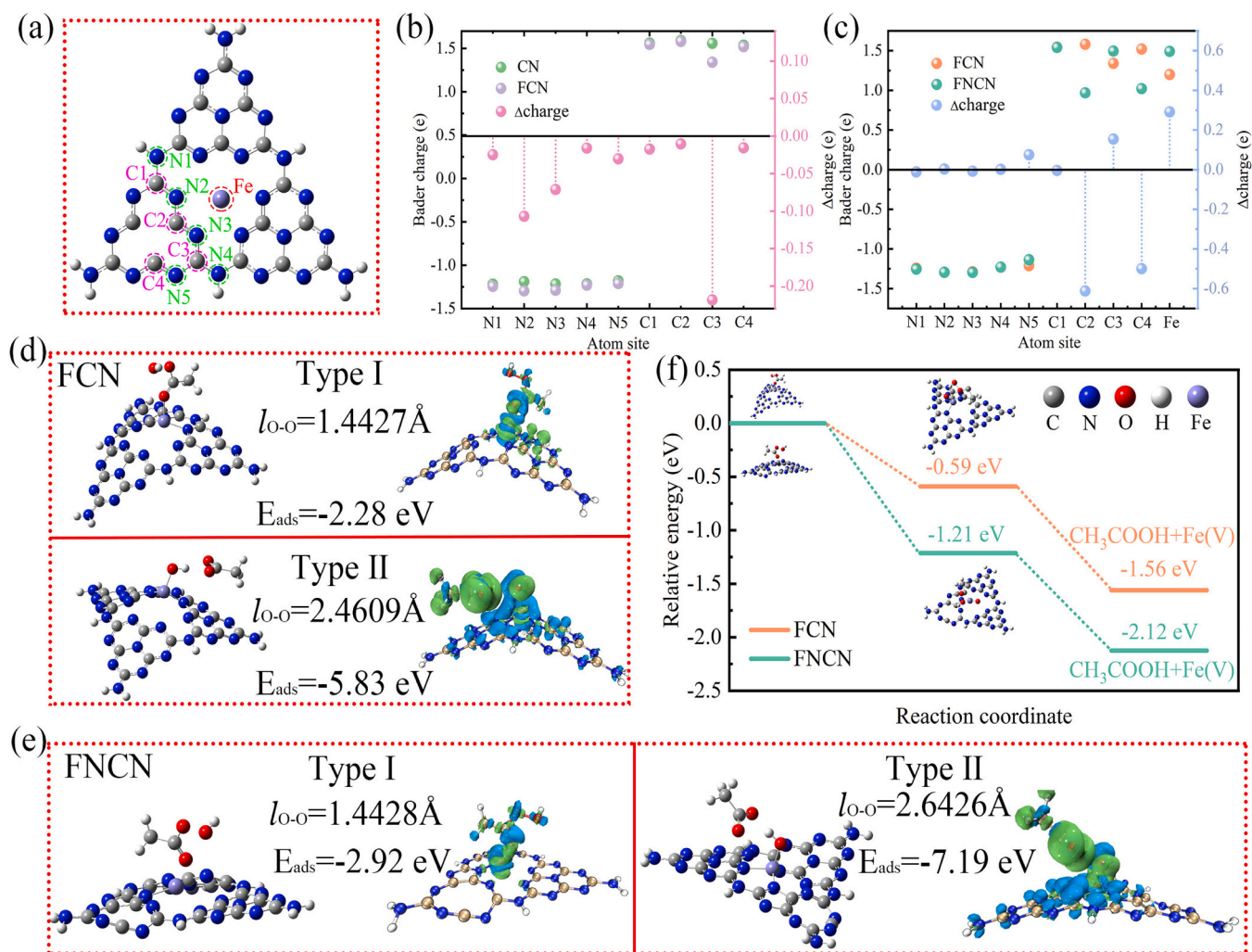


Fig. 5. (a) Structure model of FNCN. (b) Bader charge investigation between CN and FCN. (c) Bader charge investigation between FCN and FNCN. Three-dimensional charge density difference of the adsorption of PAA on different configuration in FCN (d) and FNCN (e). Green and blue denote the electron accumulation and electron depletion, respectively. (f) Energy profiles of Fe(V)=O formation for FCN and FNCN by PAA activation (inset: intermediate structures).

(Fig. S28b), FCN (Fig. 5d), and FNCN (Fig. 5e) were predicted by DFT methods. Because of their poorer connection, the virtually minimal charge transfer can be seen in the CN/PAA and NCN/PAA systems (Fig. S28). However, a large number of electron transfer was shown by the FCN/PAA and FNCN/PAA systems for boosting the PAA activation (Fig. 5d and e). The strong electron transfer between PAA and Fe sites was demonstrated by charge density difference analysis. Two possible adsorption models would occur in FNCN/PAA system, demonstrating that PAA was adsorbed at the Fe sites, and both types exhibited considerable electron transport between PAA and Fe, demonstrating that PAA chemisorption occurs at the Fe sites [61]. In type I adsorption, the Fe(III) link with the O atom in PAA close to the C atom. The interaction energies of adsorbed PAA on FCN and FNCN were -2.28 and -2.92 eV , respectively, and the O–O bond scarcely extended (1.4427 \AA for FCN and 1.4428 \AA for FNCN). Additionally, an unexpected concentration of electrons emerged on the surface of Fe sites in FCN and FNCN, demonstrating that PAA may act as the electrons donor, allowing for the delivery of electrons from PAA to the electron-acceptor region (PAA oxidation) to produce surface-bound $\text{CH}_3\text{CO}_3^\bullet$. In type II adsorption, to coordinate the Fe(III) with the O atom of PAA close to the H atom, the electron dissipation region is centered on the FCN or FNCN surface, especially on Fe sites. Meanwhile, the electron aggregation appears on the O atom of PAA near the interactive site, demonstrating a tendency of electron delivery from the Fe to PAA. At this point, the O–O bonds of

PAA are stretched to 2.46 \AA , and the adsorption energy of PAA on the FCN is -5.83 eV . For FNCN, the adsorption energy is decreased to -7.19 eV , and the O–O bonds of PAA are further stretched to 2.64 \AA . Therefore, Fe serves as the electron donor for the reduction of PAA, and the O–O bands are extended at the same time, causing PAA to spontaneously separate from the adsorption layer. Furthermore, Nvs improve the adsorption capacity of PAA on FNCN and enhance electron transfer from the FNCN catalyst surface to PAA with a tight interaction, which was also reflected by the variations in the O–O bond length of PAA.

Therefore, it is reasonable to speculate that the introduction of Nvs in FNCN can easily activate PAA to produce Fe(V)=O species, because Nvs can regulate the electron density of the Fe site in FNCN. Then, we used the calculated energy profile in Fig. 5f to trace the origin of Fe(III)-to-Fe(V)=O and to clarify the role of Nvs. PAA was initially adsorbed on the surface of the FNCN and complexed with Fe(III) to form the intermediate PAA-Fe(III). Subsequently, the O–O bond in PAA-Fe(III) was radicalized to generate a transitory state and then destroyed to spontaneously release Fe(V)=O species. For FCN and FNCN, the energy barriers during the transition from PAA-Fe(III) to Fe(V)=O species were -1.56 and -2.12 eV , respectively, indicating that the conversion from Fe(III)-to-Fe(V)=O was thermodynamically favored. The fact that ΔG of FNCN was decreased by 0.62 eV from PAA-Fe(III) to the transient state and 0.56 eV from the transient state to Fe(V)=O species compare with FCN, implying that Nvs promoted the generation of Fe(V)=O species. We

consequently realized that Nvs optimized the electron distribution of Fe (III), reduced the energy barrier, and accelerated the production of Fe (V)=O, leading to the organic substances were rapidly degraded in FNCN/PAA system.

3.5. Degradation pathways of SMX and acute toxicity estimation

To investigate the regioselectivity of active compounds, we employed the Fukui index (f^- , f^+ , f^0) of elements in SMX. Generally, the more negative the condensed dual descriptor (CDD) value indicates a greater ability of a site to supply electrons, making it more susceptible to oxidation and prone to nucleophilic reactions [62,63]. The Fe(V)=O species as a positive oxidizing agent is more likely to react with rich electronics groups. It can be clearly seen in Table S11 that C3, C6, N11, H12, and H13 have the most negative CDD values, therefore, these sites are easily attacked during the FNCN/PAA reaction. Additionally, HPLC-MS was used to determine the primary intermediate products (IPs) in the decomposition of SMX (Figs. S29 and S30). Based on the identified IPs and the CDD of SMX, the degradation pathways of SMX are proposed in Fig. 6. The amino group in SMX is an electron-rich group, so the aniline oxidation occurred in the degradation of SMX. First, Fe(V)=O species can initiate transport of the oxygen atom from the aniline ring to produce M/Z = 270. The oxidation of the amino group in the benzene ring of M/Z = 270 resulted in the formation of the intermediate product of 4-nitroso-SMX (M/Z = 268). Further oxidation of M/Z = 268 resulted in the formation of 4-nitro-SMX (M/Z = 284) and hydroxylated-4-nitro-SMX (M/Z = 300). The N-S and C-S bonds in M/Z = 268 could dissociate for further oxidation [64]. Because the electron-withdrawing properties of the sulfonamide moiety at the para position, the sulfonyl group (-SO₂NH-) was reduced to a sulfinic acid group (-SO₂H) when the N-S bond was separated [65]. The sulfinic acid group (-SO₂H) was then hydrolyzed, causing the C-S bond to be broken, resulting in the formation of M/Z = 108. Then, M/Z = 108 was further oxidized to produce M/Z = 124. Furthermore, cleavage of the N-S bond, produced the intermediate of M/Z = 172. Noticeably, some dimeric products were thought to be the degradation product of SMX by R-O•

through the coupling reaction between hydroxyl-SMX and N-centered radicals [9,50], and these IPs were easily identified in the thermal/PAA system but could not be detected during the FNCN/PAA process, further proving that R-O• had a negligible contribution to the FNCN/PAA process. The toxicity of SMX and its intermediates for animals and plants in water during the removal reaction is very important. Consequently, we predicted the toxicities of these IPs in SMX decomposition using the ECOSAR program. In Table S12, the sensitivities of daphnid, fish, and algae to SMX and its intermediates were different, with fish (Chronic toxicity) being the most vulnerable. Excluding the P1, P2, P8, P11 and P18, other molecules are extremely harmful to daphnids in considerations of chronic toxicity. Additionally, other intermediates were extremely harmful to fish in considerations of chronic toxicity, with the exception of P1, P2, P11, P14, P17, and P18. Apparently P7, P9, P15, and P16 were extreme poisonous to algae, and all other chemicals were mildly hazardous. According to the above analysis, the poisonousness of intermediates during the process of SMX removal had been substantially reformed.

4. Conclusions

This study rationally designed the Fe (III) decorated g-C₃N₄ with three coordinate nitrogen vacancies to activate PAA in the heterogeneous Fenton-like reactions. Under ideal circumstances, the highest removal rate of ~100% was achieved over 60 min in the removal of SMX by the FNCN3/PAA system. As demonstrated with these results, a non-radical mechanism of Fe(V)=O species was proposed for the oxidation of SMX, and Fe (III) sites were the primary active sites in FNCN3. Importantly, Nvs optimized the electron distribution of Fe(III) sites, reduced the energy barrier, and accelerated the production of Fe(V)=O species in PAA activation. The aforementioned improvements could facilitate the rapid degradation of organic substances in the FNCN3/PAA system. Based on this unique mechanism, this FNCN3/PAA system exhibits the feature of selectivity and anti-interference in SMX removal. FNCN3 also showed excellent durability for SMX degradation during numerous cycles. Therefore, the as-obtained FNCN3 catalyst can be a promising

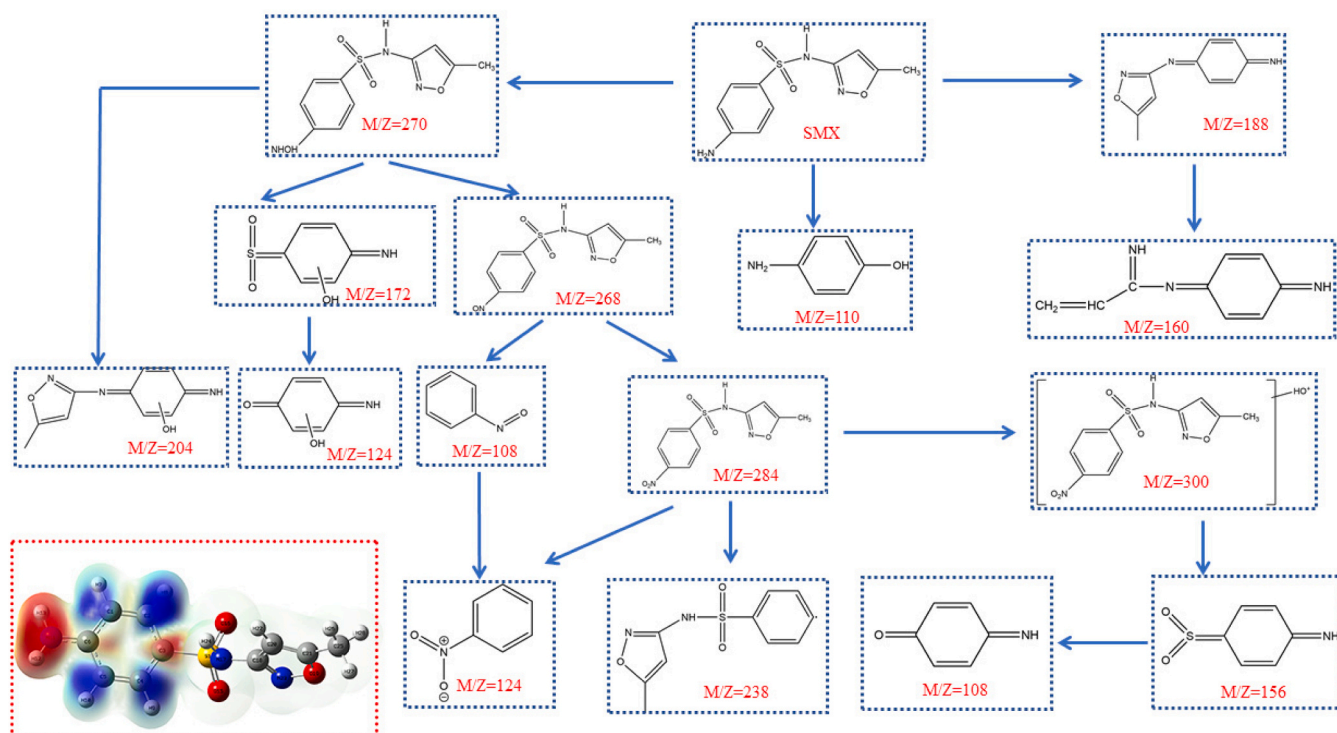


Fig. 6. Proposed pathway of SMX degradation during the FNCN3/PAA process (Contour surface of condensed dual descriptor values of SMX in red box).

material, and this study also provides a new mechanistic insight into the generation of high-valent active species assisted with defect engineering in wastewater treatment.

CRediT authorship contribution statement

Junyan Kuang: Conceptualization, Methodology, Software, Data curation, Writing – original draft, Visualization, Investigation, Software, Validation, Writing – review & editing. **Qishi Si:** Formal analysis, Visualization. **HaiJuan Guo:** Project administration, Conceptualization, Formal analysis, Funding acquisition. **Fang Ma:** Formal analysis, Visualization, Supervision, Funding acquisition. **Wanqian Guo:** Formal analysis.

Declaration of Competing Interest

The authors declare that they have no known competing financial interests or personal relationships that could have appeared to influence the work reported in this paper.

Data availability

Data will be made available on request.

Acknowledgments

This work was supported by the National Natural Science Foundation of China (Nos. 51878237 and 52070054). We would also like to acknowledge the assistance of Heilongjiang Touyan Team.

Appendix A. Supplementary material

Supplementary data associated with this article can be found in the online version at [doi:10.1016/j.apcatb.2023.122990](https://doi.org/10.1016/j.apcatb.2023.122990).

References

- [1] P. Hu, H. Su, Z. Chen, C. Yu, Q. Li, B. Zhou, P.J.J. Alvarez, M. Long, Selective degradation of organic pollutants using an efficient metal-free catalyst derived from carbonized polypyrrole via peroxymonosulfate activation, *Environ. Sci. Technol.* 51 (2017) 11288–11296.
- [2] F. Chen, G.-X. Huang, F.-B. Yao, Q. Yang, Y.-M. Zheng, Q.-B. Zhao, H.-Q. Yu, Catalytic degradation of ciprofloxacin by a visible-light-assisted peroxymonosulfate activation system: performance and mechanism, *Water Res.* 173 (2020), 115559.
- [3] J. Wang, K.-P. Hou, Y. Wen, H. Liu, H. Wang, K. Chakarawet, M. Gong, X. Yang, Interlayer structure manipulation of iron oxychloride by potassium cation intercalation to steer H_2O_2 activation pathway, *J. Am. Chem. Soc.* 144 (2022) 4294–4299.
- [4] F. Meng, J. Xu, H. Dai, Y. Yu, D. Lin, Even incorporation of nitrogen into Fe-0 nanoparticles as crystalline Fe_4N for efficient and selective trichloroethylene degradation, *Environ. Sci. Technol.* 56 (2022) 4489–4497.
- [5] S. Wang, Y. Deng, B. Shao, J. Zhu, Z. Hu, X. Guan, Three kinetic patterns for the oxidation of emerging organic contaminants by $Fe(VI)$: the critical roles of $Fe(V)$ and $Fe(IV)$, *Environ. Sci. Technol.* 55 (2021) 11338–11347.
- [6] F. Chen, L. Liu, J. Wu, X. Rui, J. Chen, Y. Yu, Single-atom iron anchored tubular $g-C_3N_4$ catalysts for ultrafast fenton-like reaction: roles of high-valency iron-oxo species and organic radicals, *Adv. Mater.* 34 (2022) 2202891.
- [7] J. Kim, C.-H. Huang, Reactivity of peracetic acid with organic compounds: a critical review, *ACS ES&T Water* 1 (2021) 15–33.
- [8] L.-W. Yang, L.-H. She, Z.-H. Xie, Y.-L. He, X.-Y. Tian, C.-L. Zhao, Y.-Q. Guo, C. Hai, C.-S. He, B. Lai, Boosting activation of peracetic acid by $Co@mZVI$ for efficient degradation of sulfamethoxazole: interesting two-phase generation of reactive oxidized species, *Chem. Eng. J.* 448 (2022), 137667.
- [9] J. Wang, Y. Wan, J. Ding, Z. Wang, J. Ma, P. Xie, M.R. Wiesner, Thermal activation of peracetic acid in aquatic solution: the mechanism and application to degrade sulfamethoxazole, *Environ. Sci. Technol.* 54 (2020) 14635–14645.
- [10] J. Wang, J. Kim, D.C. Ashley, V.K. Sharma, C.-H. Huang, Peracetic acid enhances micropollutant degradation by ferrate(VI) through promotion of electron transfer efficiency, *Environ. Sci. Technol.* 56 (2022) 11683–11693.
- [11] S. Chen, M. Cai, Y. Liu, L. Zhang, L. Feng, Effects of water matrices on the degradation of naproxen by reactive radicals in the UV/peracetic acid process, *Water Res.* 150 (2019) 153–161.
- [12] R. Bianchini, L. Calucci, C. Lubello, C. Pinzino, Intermediate free radicals in the oxidation of wastewaters, *Res. Chem. Intermed.* 28 (2002) 247–256.
- [13] J. Kim, T. Zhang, W. Liu, P. Du, J.T. Dobson, C.-H. Huang, Advanced oxidation process with peracetic acid and $Fe(II)$ for contaminant degradation, *Environ. Sci. Technol.* 53 (2019) 13312–13322.
- [14] R. Li, K. Manoli, J. Kim, M. Feng, C.-H. Huang, V.K. Sharma, Peracetic acid-ruthenium(III) oxidation process for the degradation of micropollutants in water, *Environ. Sci. Technol.* 55 (2021) 9150–9160.
- [15] J. Kim, P. Du, W. Liu, C. Lou, H. Zhao, C. Huang, Cobalt/peracetic acid: advanced oxidation of aromatic organic compounds by acetylperoxyl radicals, *Environ. Sci. Technol.* 54 (2020) 5268–5278.
- [16] D. Mandelli, Y.N. Kozlov, C.C. Golfeto, G.B. Shul'pin, Peroxyacetic acid oxidation of olefins and alkanes catalyzed by a dinuclear manganese(IV) complex with 1,4,7-trimethyl-1,4,7-triazacyclononane, *Catal. Lett.* 118 (2007) 22–29.
- [17] E.-T. Yun, H.-Y. Yoo, H. Bae, H.-I. Kim, J. Lee, Exploring the role of persulfate in the activation process: radical precursor versus electron acceptor, *Environ. Sci. Technol.* 51 (2017) 10090–10099.
- [18] J. Chen, A. Draksharapu, D. Angelone, D. Unjaroen, S.K. Padamati, R. Hage, M. Swart, C. Duboc, W.R. Browne, H_2O_2 oxidation by $Fe-III$ -OOH intermediates and its effect on catalytic efficiency, *ACS Catal.* 8 (2018) 9665–9674.
- [19] C.K. Remucal, D.L. Sedlak, The role of iron coordination in the production of reactive oxidants from ferrous iron oxidation by oxygen and hydrogen peroxide, in: *Proceedings of the 239th National Meeting of the American-Chemical-Society* San Francisco, CA, 2010, p. 177.
- [20] W.-D. Oh, V.W.C. Chang, Z.-T. Hu, R. Goei, T.-T. Lim, Enhancing the catalytic activity of $g-C_3N_4$ through Me doping (Me = Cu, Co and Fe) for selective sulfathiazole degradation via redox-based advanced oxidation process, *Chem. Eng. J.* 323 (2017) 260–269.
- [21] S. Hu, X. Chen, Q. Li, F. Li, Z. Fan, H. Wang, Y. Wang, B. Zheng, G. Wu, Fe^{3+} doping promoted N_2 photofixation ability of honeycombed graphitic carbon nitride: the experimental and density functional theory simulation analysis, *Appl. Catal. B Environ.* 201 (2017) 58–69.
- [22] M. Xie, J. Tang, L. Kong, W. Lu, V. Natarajan, F. Zhu, J. Zhan, Cobalt doped $g-C_3N_4$ activation of peroxymonosulfate for monochlorophenols degradation, *Chem. Eng. J.* 360 (2019) 1213–1222.
- [23] H. Li, C. Shan, B. Pan, $Fe(III)$ -doped $g-C_3N_4$ mediated peroxymonosulfate activation for selective degradation of phenolic compounds via high-valent iron-oxo species, *Environ. Sci. Technol.* 52 (2018) 2197–2205.
- [24] B. Liu, W. Guo, W. Jia, H. Wang, Q. Si, Q. Zhao, H. Luo, J. Jiang, N. Ren, Novel nonradical oxidation of sulfonamide antibiotics with $Co(II)$ -doped $g-C_3N_4$ -activated peracetic acid: role of high-valent cobalt-oxo species, *Environ. Sci. Technol.* 55 (2021) 12640–12651.
- [25] N. Jiang, H. Xu, L. Wang, J. Jiang, T. Zhang, Nonradical oxidation of pollutants with single-atom- $Fe(III)$ -activated persulfate: $Fe(V)$ being the possible intermediate oxidant, *Environ. Sci. Technol.* 54 (2020) 14057–14065.
- [26] N. Li, W. Lu, K. Pei, Y. Yao, W. Chen, Formation of high-valent cobalt-oxo phthalocyanine species in a cellulose matrix for eliminating organic pollutants, *Appl. Catal. B Environ.* 163 (2015) 105–112.
- [27] Y. Zong, X. Guan, J. Xu, Y. Feng, Y. Mao, L. Xu, H. Chu, D. Wu, Unraveling the overlooked involvement of high-valent cobalt-oxo species generated from the cobalt(II)-activated peroxymonosulfate process, *Environ. Sci. Technol.* 54 (2020) 16231–16239.
- [28] Y. Zong, Y. Shao, Y. Zeng, B. Shao, L. Xu, Z. Zhao, W. Liu, D. Wu, Enhanced oxidation of organic contaminants by iron(II)-activated periodate: the significance of high-valent iron-oxo species, *Environ. Sci. Technol.* 55 (2021) 7634–7642.
- [29] Y. Zong, H. Zhang, X. Zhang, W. Liu, L. Xu, D. Wu, High-valent cobalt-oxo species triggers hydroxyl radical for collaborative environmental decontamination, *Appl. Catal. B Environ.* 300 (2022), 120722.
- [30] C.-W. Zheng, H.-Y. Niu, C. Liang, C.-G. Niu, X.-F. Zhao, L. Zhang, J.-S. Li, H. Guo, H.-Y. Liu, S. Liang, A study on advanced oxidation mechanism of $MnCo_2O_4/g-C_3N_4$ degradation of nitrobenzene: sacrificial oxidation and radical oxidation, *Chem. Eng. J.* 403 (2021), 126400.
- [31] J. Jiang, X. Wang, C. Yue, T. Li, M. Li, C. Li, S. Dong, Nitrogen vacancies induce sustainable redox of iron-cobalt bimetal for efficient peroxymonosulfate activation: dual-path electron transfer, *Chem. Eng. J.* 427 (2022), 131702.
- [32] W. Wang, Y. Liu, Y. Yue, H. Wang, G. Cheng, C. Gao, C. Chen, Y. Ai, Z. Chen, X. Wang, The confined interlayer growth of ultrathin two-dimensional Fe_3O_4 nanosheets with enriched oxygen vacancies for peroxymonosulfate activation, *ACS Catal.* 11 (2021) 11256–11265.
- [33] Y. Duan, Y. Wang, L. Gan, J. Meng, Y. Feng, K. Wang, K. Zhou, C. Wang, X. Han, X. Zhou, Amorphous carbon nitride with three coordinate nitrogen (N_3C) vacancies for exceptional NO_x abatement in visible light, *Adv. Energy Mater.* 11 (2021) 2004001.
- [34] X. Zhang, P. Ma, C. Wang, L. Gan, X. Chen, P. Zhang, Y. Wang, H. Li, L. Wang, X. Zhou, K. Zheng, Unraveling the dual defect sites in graphite carbon nitride for ultra-high photocatalytic H_2O_2 evolution, *Energy Environ. Sci.* 15 (2022) 830–842.
- [35] L. Su, P. Wang, X. Ma, J. Wang, S. Zhan, Regulating local electron density of iron single sites by introducing nitrogen vacancies for efficient photo-fenton process, *Angew. Chem. Int. Ed.* 60 (2021) 21261–21266.
- [36] C. Lv, Y. Qian, C. Yan, Y. Ding, Y. Liu, G. Chen, G. Yu, Defect engineering metal-free polymeric carbon nitride electrocatalyst for effective nitrogen fixation under ambient conditions, *Angew. Chem. Int. Ed.* 57 (2018) 10246–10250.
- [37] T. Zhang, Y. Wen, Z. Pan, Y. Kuwahara, K. Mori, H. Yamashita, Y. Zhao, X. Qian, Overcoming acidic $H_2O_2/Fe(II/III)$ redox-induced low H_2O_2 utilization efficiency by carbon quantum dots fenton-like catalysis, *Environ. Sci. Technol.* 56 (2022) 2617–2625.
- [38] J. Kuang, Z. Xing, J. Yin, Z. Li, Q. Zhu, W. Zhou, Surface plasma Ag-decorated single-crystalline $TiO_{2-x}(B)$ nanorod/defect-rich $g-C_3N_4$ nanosheet ternary

- superstructure 3D heterojunctions as enhanced visible-light-driven photocatalyst, *J. Colloid Interface Sci.* 542 (2019) 63–72.
- [39] K. Chu, Q. Li, Y. Liu, J. Wang, Y. Cheng, Filling the nitrogen vacancies with sulphur dopants in graphitic C₃N₄ for efficient and robust electrocatalytic nitrogen reduction, *Appl. Catal. B Environ.* 267 (2020), 118693.
- [40] X. Wang, X. Chen, A. Thomas, X. Fu, M. Antonietti, Metal-containing carbon nitride compounds: a new functional organic-metal hybrid material, *Adv. Mater.* 21 (2009) 1609.
- [41] H. Yu, R. Shi, Y. Zhao, T. Bian, Y. Zhao, C. Zhou, G.I.N. Waterhouse, L.-Z. Wu, C.-H. Tung, T. Zhang, Alkali-assisted synthesis of nitrogen deficient graphitic carbon nitride with tunable band structures for efficient visible-light-driven hydrogen evolution, *Adv. Mater.* 29 (2017) 1605148.
- [42] Y. Kang, Y. Yang, L.-C. Yin, X. Kang, G. Liu, H.-M. Cheng, An amorphous carbon nitride photocatalyst with greatly extended visible-light-responsive range for photocatalytic hydrogen generation, *Adv. Mater.* 27 (2015) 4572–4577.
- [43] Y. Wang, L. Rao, P. Wang, Z. Shi, L. Zhang, Photocatalytic activity of N-TiO₂/O-doped N vacancy g-C₃N₄ and the intermediates toxicity evaluation under tetracycline hydrochloride and Cr(VI) coexistence environment, *Appl. Catal. B Environ.* 262 (2020), 118308.
- [44] Y. Gao, Y. Zhu, L. Lyu, Q. Zeng, X. Xing, C. Hu, Electronic structure modulation of graphitic carbon nitride by oxygen doping for enhanced catalytic degradation of organic pollutants through peroxymonosulfate activation, *Environ. Sci. Technol.* 52 (2018) 14371–14380.
- [45] W. Cui, J. Li, F. Dong, Y. Sun, G. Jiang, W. Cen, S.C. Lee, Z. Wu, Highly efficient performance and conversion pathway of photocatalytic NO oxidation on SrO-clusters@amorphous carbon nitride, *Environ. Sci. Technol.* 51 (2017) 10682–10690.
- [46] G. Dong, D. Jacobs, L. Zang, C. Wang, Carbon vacancy regulated photoreduction of NO to N₂ over ultrathin g-C₃N₄ nanosheets, *Appl. Catal. B Environ.* 218 (2017) 515–524.
- [47] J. Liao, J. Qiu, G. Wang, R. Du, N. Tsidaeva, W. Wang, 3D core-shell Fe₃O₄@SiO₂@MoS₂ composites with enhanced microwave absorption performance, *J. Colloid Interface Sci.* 604 (2021) 537–549.
- [48] Y. Bo, H. Wang, Y. Lin, T. Yang, R. Ye, Y. Li, C. Hu, P. Du, Y. Hu, Z. Liu, R. Long, C. Gao, B. Ye, L. Song, X. Wu, Y. Xiong, Altering hydrogenation pathways in photocatalytic nitrogen fixation by tuning local electronic structure of oxygen vacancy with dopant, *Angew. Chem. Int. Ed.* 60 (2021) 16085–16092.
- [49] B. Liu, W. Guo, W. Jia, H. Wang, S. Zheng, Q. Si, Q. Zhao, H. Luo, J. Jiang, N. Ren, Insights into the oxidation of organic contaminants by Co(II) activated peracetic acid: the overlooked role of high-valent cobalt-oxo species, *Water Res.* 201 (2021), 117313.
- [50] J. Kim, P. Du, W. Liu, C. Luo, H. Zhao, C.-H. Huang, Cobalt/peracetic acid: advanced oxidation of aromatic organic compounds by acetylperoxyl radicals, *Environ. Sci. Technol.* 54 (2020) 5268–5278.
- [51] Z. Wang, J. Wang, B. Xiong, F. Bai, S. Wang, Y. Wan, L. Zhang, P. Xie, M. R. Wiesner, Application of cobalt/peracetic acid to degrade sulfamethoxazole at neutral condition: efficiency and mechanisms, *Environ. Sci. Technol.* 54 (2020) 464–475.
- [52] A. Mortensen, Scavenging of acetylperoxyl radicals and quenching of triplet diacetyl by beta-carotene: mechanisms and kinetics, *J. Photochem. Photobiol. B Biol.* 61 (2001) 62–67.
- [53] L. Wang, W. Lu, D. Ni, T. Xu, N. Li, Z. Zhu, H. Chen, W. Chen, Solar-initiated photocatalytic degradation of carbamazepine on excited-state hexadecachlorophthalocyanine in the presence of peroxymonosulfate, *Chem. Eng. J.* 330 (2017) 625–634.
- [54] A. Ghosh, D.A. Mitchell, A. Chanda, A.D. Ryabov, D.L. Popescu, E.C. Upham, G. J. Collins, T.J. Collins, Catalase-peroxidase activity of iron(III)-TAML activators of hydrogen peroxide, *J. Am. Chem. Soc.* 130 (2008) 15116–15126.
- [55] Y. Zhou, J. Jiang, Y. Gao, J. Ma, S.-Y. Pang, J. Li, X.-T. Lu, L.-P. Yuan, Activation of peroxymonosulfate by benzoquinone: a novel nonradical oxidation process, *Environ. Sci. Technol.* 49 (2015) 12941–12950.
- [56] X. Xue, K. Hanna, C. Despas, F. Wu, N. Deng, Effect of chelating agent on the oxidation rate of PCP in the magnetite/H₂O₂ system at neutral pH, *J. Mol. Catal. A Chem.* 311 (2009) 29–35.
- [57] Y.-Y. Ahn, H. Bae, H.-I. Kim, S.-H. Kim, J.-H. Kim, S.-G. Lee, J. Lee, Surface-loaded metal nanoparticles for peroxymonosulfate activation: efficiency and mechanism reconnaissance, *Appl. Catal. B Environ.* 241 (2019) 561–569.
- [58] H. Wang, W. Guo, B. Liu, Q. Si, H. Luo, Q. Zhao, N. Ren, Sludge-derived biochar as efficient persulfate activators: sulfuration-induced electronic structure modulation and disparate nonradical mechanisms, *Appl. Catal. B Environ.* 279 (2020), 119361.
- [59] H. Wang, W. Guo, B. Liu, Q. Wu, H. Luo, Q. Zhao, Q. Si, F. Sseguya, N. Ren, Edge-nitrogenated biochar for efficient peroxydisulfate activation: an electron transfer mechanism, *Water Res.* 160 (2019) 405–414.
- [60] B. Sun, W. Ma, N. Wang, P. Xu, L. Zhang, B. Wang, H. Zhao, K.-Y.A. Lin, Y. Du, Polyaniline: a new metal-free catalyst for peroxymonosulfate activation with highly efficient and durable removal of organic pollutants, *Environ. Sci. Technol.* 53 (2019) 9771–9780.
- [61] C. Chu, J. Yang, X. Zhou, D. Huang, H. Qi, S. Weon, J. Li, M. Elimelech, A. Wang, J.-H. Kim, Cobalt single atoms on tetrapyrromacrocyclic support for efficient peroxymonosulfate activation, *Environ. Sci. Technol.* 55 (2021) 1242–1250.
- [62] Q. Si, W. Guo, H. Wang, B. Liu, S. Zheng, Q. Zhao, H. Luo, N. Ren, T. Yu, Difunctional carbon quantum dots/g-C₃N₄ with in-plane electron buffer for intense tetracycline degradation under visible light: tight adsorption and smooth electron transfer, *Appl. Catal. B Environ.* 299 (2021), 120694.
- [63] Q. Si, W. Guo, B. Liu, H. Wang, S. Zheng, Q. Zhao, H. Luo, N. Ren, T. Yu, Spin-states-assistance peroxymonosulfate absorption via Mn doped catalyst with/without light for BPA oxidation: the negative contribution of electrons transfer by light, *Chem. Eng. J.* 443 (2022), 136399.
- [64] Z. Yin, M. Cai, X. Weng, Z. Liu, G. Zhang, Porcine insulin receptor substrate 2: molecular cloning, tissues distribution, and functions in hepatocyte and aortic endothelial cells, *Pol. J. Vet. Sci.* 22 (2019) 589–598.
- [65] Y. Ji, Y. Fan, K. Liu, D. Kong, J. Lu, Thermo activated persulfate oxidation of antibiotic sulfamethoxazole and structurally related compounds, *Water Res.* 87 (2015) 1–9.